Hardware-in-the-Loop Emulator Test-Setup for a Dual-Rotor Contra-Rotating Pump-Turbine

Truijen, Daan P.K.; Hoffstaedt, Justus P.; Fahlbeck, Jonathan; Jarquin-Laguna, Antonio; Nilsson, Håkan; Stockman, Kurt; De Kooning, Jeroen D.M.

DOI
10.1049/icp.2024.2140

Publication date
2024

Document Version
Final published version

Published in
IET Conference Proceedings

Hardware-in-the-Loop Emulator Test-Setup for a Dual-Rotor Contra-Rotating Pump-Turbine

Daan P. K. Truijen[1,2], Justus P. Hoffstaedt[3], Jonathan Fahlbeck[4], Antonio Jarquin-Laguna[3], Håkan Nilsson[4], Kurt Stockman[1,2], Jeroen D. M. De Kooning[1,2]*

[1]*Department of Electromechanical, Systems & Metal Engineering, Ghent University, Ghent, Belgium*
[2]*FlandersMake@UGent - Corelab MIRO, Flanders Make, Belgium*
[3]*Department of Maritime and Transport Technology, Delft University of Technology, Delft, the Netherlands*
[4]*Department of Mechanics and Maritime Sciences, Chalmers University of Technology, Gothenburg, Sweden*
**E-mail: daan.truijen@ugent.be*

Keywords: HIL EMULATOR TEST-SETUP, PUMPED HYDROPOWER STORAGE, AXIAL-FLUX PMSM, ENERGY STORAGE

Abstract

Recently, contra-rotating reversible pump-turbines (CR RPTs) have been proposed to increase the efficiency of low-head pumped hydropower storage applications, which are promising to provide energy storage for non-mountainous regions. To study the control architectures for these systems, a dual-rotor hardware-in-the-loop (HIL) emulator test-setup is developed. The HIL test-setup employs two induction machines controlled by separate regenerative variable frequency drives to emulate the torques on the two runners. A quasi-steady-state RPT model is developed based on 380 steady-state computational fluid dynamics (CFD) simulations and compared to three transient CFD simulations to analyse the dynamics. Furthermore, the runner torques are adapted to account for the lower friction and higher inertia of the HIL test-setup compared to the prototype CR RPT, ensuring accurate emulation. Finally, it is shown how precise calibration of the drive torque response averts torque errors related to the machine model estimator used in direct torque control. The developed emulator setup offers a cost-effective and controlled environment to optimise and validate control architectures for the novel CR RPT, providing a higher fidelity than theoretical simulation by including the physical effects of the drivetrain, electrical machines and converters that are not entirely captured in mathematical models.

1 Introduction

Hardware-in-the-loop (HIL) emulator test-setups are increasingly used to study the dynamic behaviour of complex systems, such as wind and hydropower (pump-)turbines. These HIL test-setups emulate the characteristics and dynamic behaviour of pump-turbines, offering a cost-effective and controlled environment for experimentation to analyse different control architectures. Unlike traditional simulations that rely solely on mathematical models, HIL emulators integrate physical hardware components into the simulation loop, enhancing the fidelity of the simulation by capturing dynamics and uncertainties that are not included in pure simulation.

In this paper, the design and development of an emulator test-setup is described for a novel contra-rotating reversible pump-turbine (CR RPT). Here, the RPT comprises two runners with opposite rotational motion, limiting the creation of swirl and increasing the efficiency and improving pump stability [1, 2]. This novel axial RPT was designed to enable pumped hydropower storage (PHS) technologies for low-head applications, where the flow rate is typically large [3]. In this HIL emulator test-setup, two induction machines, controlled with separate fully regenerative variable frequency drives (VFDs) are controlled to emulate the RPT torques on the two runners. These emulator machines are coupled to axial-flux permanent magnet synchronous machines (AF-PMSMs), that serve as the motor-generator units, on which different control architectures and operational scenarios can be tested. These AF-PMSMs are also envisioned for prospective full-scale prototypes of the novel low-head PHS systems, as they have a high efficiency and power density compared to classical radial-flux machines [2, 4].

To accurately emulate the RPT, its characteristics and dynamics are modelled using extensive computational fluid dynamics (CFD) simulations over the full operating range [3]. Here, the main challenge is the correct emulation of the interaction between both runners through the fluid. The strength of this HIL test-setup is a parallel physical hydraulic test-setup, featuring an actual conduit and RPT prototype, which is developed to perform the CFD validation. This hydraulic setup matches the HIL emulator setup and is pictured Fig 1 and outlined in [5]. The RPT used in this setup is a scaled-down version of a 10 MW system [3]. The synergy between the emulator and a hydraulic test-setup, featuring an actual prototype RPT, provides a unique opportunity for thorough validation. This dual approach allows the physical test results to be used to optimise the RPT emulator model in a time-efficient way, while the HIL setup is used to explore new control architectures and operational scenarios.

In literature, numerous HIL setups have been described for hydropower [6–9] and wind turbines [10–12]. To account for the difference in inertia between the emulating and emulated

https://doi.org/10.1049/icp.2024.2140

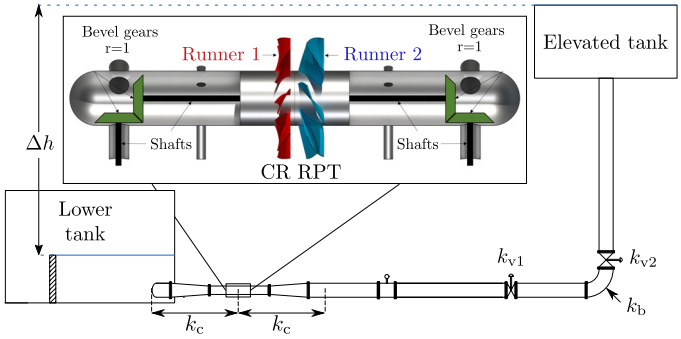

Fig. 1 Overview of the hydraulic test-setup conduit, with CR RPT location and mounting arrangement highlighted and local loss locations indicated.

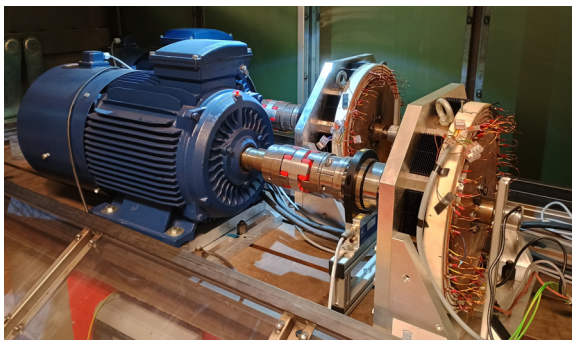

Fig. 2 The HIL emulator test-setup induction machines and AF-PMSMs.

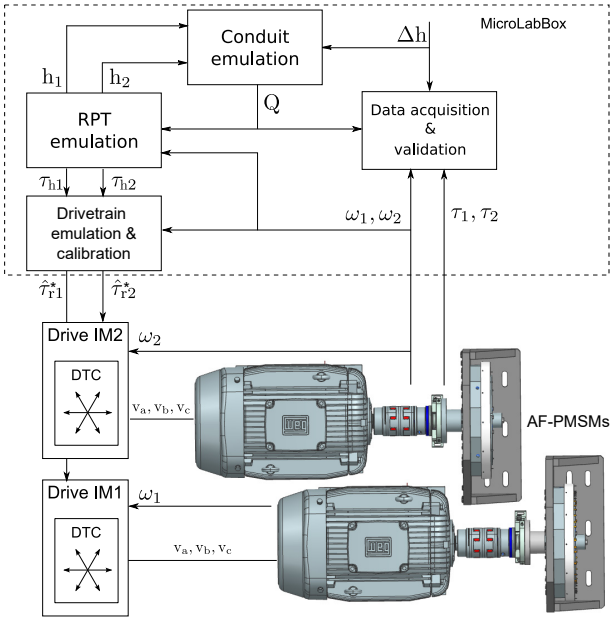

Fig. 3 Schematic overview of the test-setup and control interface, with control signals and sensor measurements indicated.

device, [8] and [11] use a mechanical flywheel. While this approach has optimal performance, it is not easily configurable and cannot be used to emulate an inertia below the physical inertia in the emulator test-setup. In [6, 8, 10, 12, 13], the inertia is implemented by simulating the emulated drivetrain speed based on the turbine torque and measured generator torque and then feeding this to a speed controller on the emulator. The speed tracking error in this speed controller limits the accuracy of this method in dynamic scenarios. Therefore, in the developed emulator setup in this paper, a correcting inertia and friction torque is added to the emulator torque to provide accurate emulation.

In Section 2, the test-setup and its components are outlined, followed by a description of the RPT and conduit modelling. Next, the emulation of friction and inertia is described in Section 4.1. To ensure accurate emulation, a torque response calibration of the direct torque control (DTC) used in the VFDs is described in Section 4.2. Finally, the emulation results of a general test case are presented in Section 5.

2 Test-Setup Overview

Fig. 2 shows the components of the HIL test-setup. Two four-pole induction machines (IMs) of 37 kW, 1500 rpm with forced air cooling are used to emulate the CR RPT runners. The IMs are driven by two separate fully regenerative ABB-ACS880-11 72A VFDs, to be able to emulate in both pump and turbine mode. Next, the IMs are mechanically coupled to their respective (32 kW, 1500 rpm) AF-PMSMs through a double-cardanic ROTEX GS DKM backlash-free coupling. On each drivetrain, an HBK T40B 500 N·m torque sensor is used to validate the emulator behaviour, AF-PMSM design and control architecture. These torque sensors have an accuracy class of 0.05% M_n, a temperature effect of $\pm 0.5\%$ $^{M_n}/_{10K}$ and a frequency output signal of $5 - 15$ kHz, which can be read by the central controller with minimal latency and conversion errors. A dSpace MicroLabBox is used as the central controller for data-acquisition and control of the RPT emulation. The induction machines are equipped with incremental encoders with 1024 pulses per revolution with differential TTL signals to measure the rotational speed, which is fed back to the ABB drives and the MicroLabBox.

A schematic overview of the control interface with indicated control signals and sensor measurements is shown in Fig. 3. Based on the measured rotational speeds $\omega_{1,2}$ of both runners, the RPT emulation calculates the RPT runner heads $h_{1,2}$. This allows the conduit emulation to calculate the flow rate Q for a given fallhead between the reservoirs Δh. With Q known, the RPT runner torques $\tau_{h1,2}$ are calculated. Next, the friction and inertia torques are added and sent as torque setpoints $\hat{\tau}_{r1,2}$ to the ABB drives to emulate the RPT torques. In parallel, the MicroLabBox performs the data-acquisition, running at a sample time of 1 ms.

3 Reversible Pump-Turbine Emulation

3.1 Quasi Steady-State Model

The CR RPT characterisation is based on a range of 380 steady-state CFD simulations. The CFD simulations are performed using the foam-extend revision 2d9985 (4.1 nextRelease). Turbulence is modelled using the k-ω shear stress transport two equation eddy-viscosity model. The numerical domain consists of one blade passage per runner with a total of $1.3 \cdot 10^6$ cells. To emulate the full runners, cyclic boundaries and a mixing-plane between the runners are used. The runner rotation is modelled using the multiple reference frames approach. The RPT has, respectively in pump and turbine mode, nominal flow rates of $Q = 0.37$ m³/s and 0.29 m³/s, nominal powers of $P_\mathrm{r} = 48.3$ kW and 15.3 kW for both runners combined, and nominal hydraulic efficiencies of $\eta_\mathrm{h} = 88.9\%$ and 90.3%. To characterise the runners, the net head $h_{1,2}$ of the runners are adimensionalised by dividing with the dynamic head (1). The resulting pressure head coefficients $C_{h1,2}$ as well as the efficiencies $\eta_{h1,2}$ are described as a function of both tip speed ratios $\lambda_{1,2}$. The tip speed ratio is defined as the tangential velocity of the runner tips $R\,\omega_{1,2}$ divided by the average flow velocity Q/A (2). Here, R and A are the runner radius and area respectively.

$$C_{h1,2} = \frac{g\,h_{1,2}}{\frac{1}{2}(Q/A)^2} \quad (1) \qquad \lambda_{1,2} = \frac{R\,\omega_{1,2}}{Q/A} \quad (2)$$

Figure 4 shows the curves for $C_{h1,2}$ and $\eta_{h1,2}$ in both pump and turbine mode with each line representing different speed ratios $\zeta = \omega_2/\omega_1$, ranging from $0.70 \leq \zeta \leq 1.00$ in turbine mode and $0.70 \leq \zeta \leq 1.15$ in pump mode. As the RPT characteristics are highly non-linear (especially in pump mode), 2D-lookup tables with linear interpolation, based on the aforementioned steady-state CFD simulations, are used to define $C_{h1,2}$ and $\eta_{h1,2}$. The stability limits for the tip speed ratios λ are a function of the speed ratios ζ. Finally, the simulated hydraulic torque $\tau_{\mathrm{h}1,2}$ is calculated using (3) in turbine mode. In pump mode, $\eta_{h1,2}$ is placed in the denominator instead of the numerator.

$$\tau_{\mathrm{h}1,2} = \frac{\rho\,g\,Q\,h_{1,2}\,\eta_{h1,2}}{\omega_{1,2}} \text{ (turbine)} \quad (3)$$

The losses that occur in the conduit (Fig. 1) can be divided into the major losses, occurring due to friction in the conduit and the local minor losses, occurring e.g. at the conduit entrance, exit, and the valves. The conduit dimensions and parameters are listed in Table 1. The major losses are calculated using the Darcy-Weisbach formula (4), where the friction factor $f(x)$ is approximated by the Colebrook-White equation for turbulent flow (5).

$$h_{\mathrm{L,M}} = \int_0^L f(x)\frac{1}{D(x)}\frac{v^2(x)}{2g}\,dx \quad (4)$$

$$\frac{1}{\sqrt{f(x)}} = -2\log\left(\frac{e}{3.7 \cdot D(x)}\right) \quad (5)$$

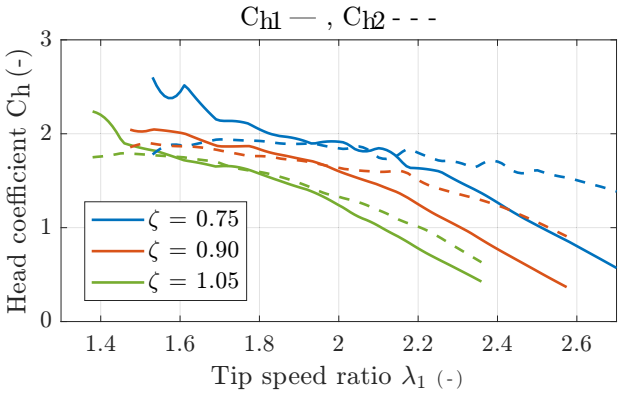

(a) Head coefficients in turbine mode.

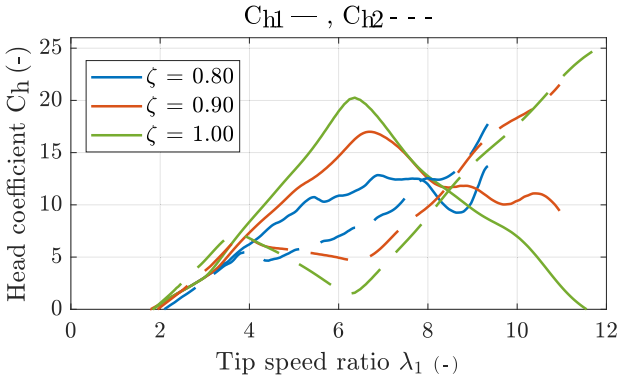

(b) Head coefficients in pump mode.

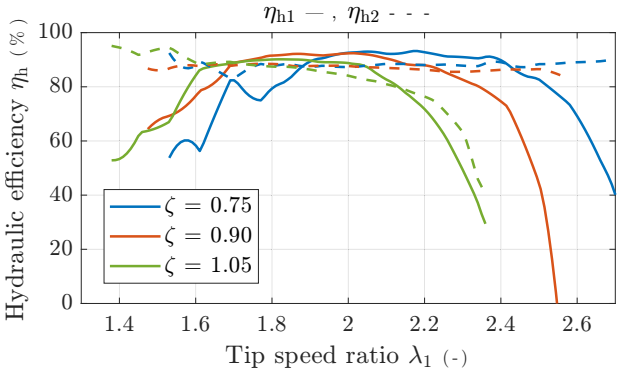

(c) Efficiencies in turbine mode.

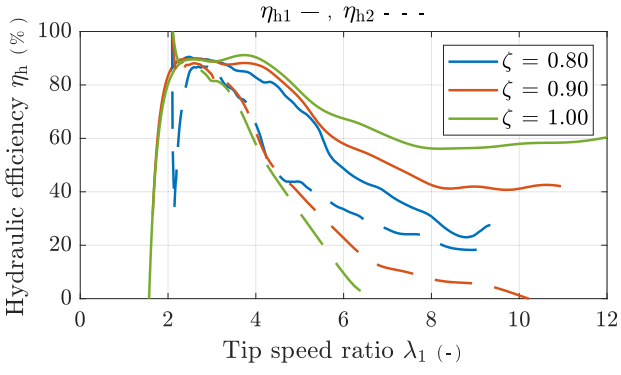

(d) Efficiencies in pump mode.

Fig. 4 RPT head coefficients $C_{h1,2}$ and efficiency $\eta_{h1,2}$ versus tip speed ratios $\lambda_{1,2}$ for different speed ratios ζ.

Here, x is the horizontal distance from the left reservoir entrance, L is the total conduit length, $v(x)$ is the flow velocity, $D(x)$ is the conduit diameter, g is the gravity constant, and e is the relative roughness of the conduit. Finally, the minor losses are calculated in (6). In this equation, k_i are the minor loss coefficients, listed in Table 1. k_c is the minor loss coefficient of the CFD domain, including the CR RPT and draft tubes (see Fig. 1). The CFD domain is symmetrical and both sides have a coefficient of 5.21.

$$h_{\mathrm{L,m}} = \sum_i k_i \frac{v^2(x_i)}{2g} \tag{6}$$

Table 1 Conduit parameters used for the simulations.

Conduit dimensions		
Conduit length	L [m]	16.05
Conduit diameter	D [m]	0.5
Relative roughness	e [mm]	0.05
Minor loss coefficients		
Entrance	k_{en} [-]	0.45
Exit	k_{ex} [-]	1
CFD domain	k_{c} [-]	5.21
90° bend	k_{b} [-]	0.2
Open-close valve	k_{v2} [-]	0.4
Flow-control valve	k_{v1} [-]	0.39

3.2 Quasi Steady-State Model Dynamics

Next to the steady-state CFD simulations, three transient simulations have been performed in pump mode, which can be used to analyse the QSS model performance in dynamic scenarios. These simulations are performed using the OpenFOAM-v2112 CFD code. Turbulence is modelled using the k-ω shear stress transport - scale adaptive simulation (SAS) two equation eddy-viscosity model. The SAS modifications allow for a local decrease in the turbulent viscosity. Turbulence is thus resolved in parts of the numerical domain. The mesh, with a total of $12 \cdot 10^6$ cells, is divided into four parts, one for each of the runners, and one region on each side of the runners. In the simulations, the runners are rotating by prescribing a solid body rotation to the mesh regions of the runners. The headLossPressure [14] boundary condition is used to achieve flow driving pressure differences by characterising the full system shown in Fig. 1. Fig. 5 shows how the flow rate and hydraulic torques compare for the described QSS model and the CFD simulations for the three transient cases. The fallhead in these cases is $\Delta h = 6.45$ m. It is seen that for all cases, the flow rate and first runner torque simulations of the QSS model represent the CFD outcomes well. However, consistent variances are observed. The flow rate decrease initiates faster in the QSS model than in the CFD model, while it reaches steady-state slightly slower compared to the CFD model. For the second runner torque, a larger error exists for the QSS model. These differences become most apparent during deceleration, but are also present when the rotational speeds are constant, with average errors of 3.2%, 3.7% and 2.1%. A possible explanation for this error is the lower fidelity of the steady-state CFD simulations used for characterisation, which affect the torque prediction of the downstream (second) runner due to flow separation that is not fully captured.

Although the QSS model represents the system well in these transient scenarios, the consistent variances may be able to be captured in a data-driven model. While three transient CFD simulations are not sufficient to characterise the dynamics over the full operating range, transient tests are planned at the hydraulic test-setup in both pump and turbine mode. In future work, the results of these tests will be used to train an appropriate data-driven model that complements the QSS model in dynamic operation, e.g. a non-linear autoregressive with exogenous input (NLARX) model.

4 Drivetrain

4.1 Friction and Inertia emulation

To accurately emulate the friction and inertia of the RPT and drivetrain in the hydraulic test-setup, the first order motion equations for both the hydraulic (7) and the emulator setup (8) are combined to find the emulator runner torques $\tau_{\mathrm{r}1,2}$ for the induction machines in (9). Here, J is the rotational inertia, τ_{f} is the friction torque, τ_{r} is the runner torque (emulated by the induction machines) and τ_{m} is the AF-PMSM torque. The subscripts a and b respectively denote the hydraulic test-setup and the emulator test-setup.

$$\text{Hydraulic setup: } J_{\mathrm{a}} \frac{d\omega}{dt} = \tau_{\mathrm{h}} - \tau_{\mathrm{m}} - \tau_{\mathrm{fa}} \tag{7}$$

$$\text{Emulator setup: } J_{\mathrm{b}} \frac{d\omega}{dt} = \tau_{\mathrm{r}} - \tau_{\mathrm{m}} - \tau_{\mathrm{fb}} \tag{8}$$

$$\Rightarrow \tau_{\mathrm{r}} = \tau_{\mathrm{h}} + (J_{\mathrm{b}} - J_{\mathrm{a}}) \frac{d\omega}{dt} + (\tau_{\mathrm{fb}} - \tau_{\mathrm{fa}}) \tag{9}$$

Based on an initial characterisation test in the hydraulic test-setup (experiment C_DF_D1 in [5]), the friction torques are modelled with a static friction component and a viscous friction component which is linearly proportional to the rotational speed in (10), where coefficients $\alpha_{1,2}$ and $\beta_{1,2}$ are listed in Table 2. In the emulator setup, the friction in each drivetrain is the sum of the friction in the IM and the AF-PMSM. The friction of one machine is found by actuating the other machine in constant speed control (with steps of $\Delta\omega = 5.24$ rad/s) and analysing the torque sensor measurement. This characterisation is saved in a 1D-lookup table with linear interpolation. The characterisation of both the hydraulic and emulator test-setups is visualised in Fig. 6. Note that the friction torques in the hydraulic test-setup are significantly higher than those of the emulator test-setup. Therefore, according to (9), the emulator torques adjust accordingly based on the measured rotational speed and thus reduces its runner torque $\tau_{\mathrm{r}1,2}$ to account for the higher friction.

$$\tau_{\mathrm{fa}1,2} = \alpha_{1,2} \cdot \omega_{1,2} + \mathrm{sign}(\omega_{1,2}) \cdot \beta_{1,2} \tag{10}$$

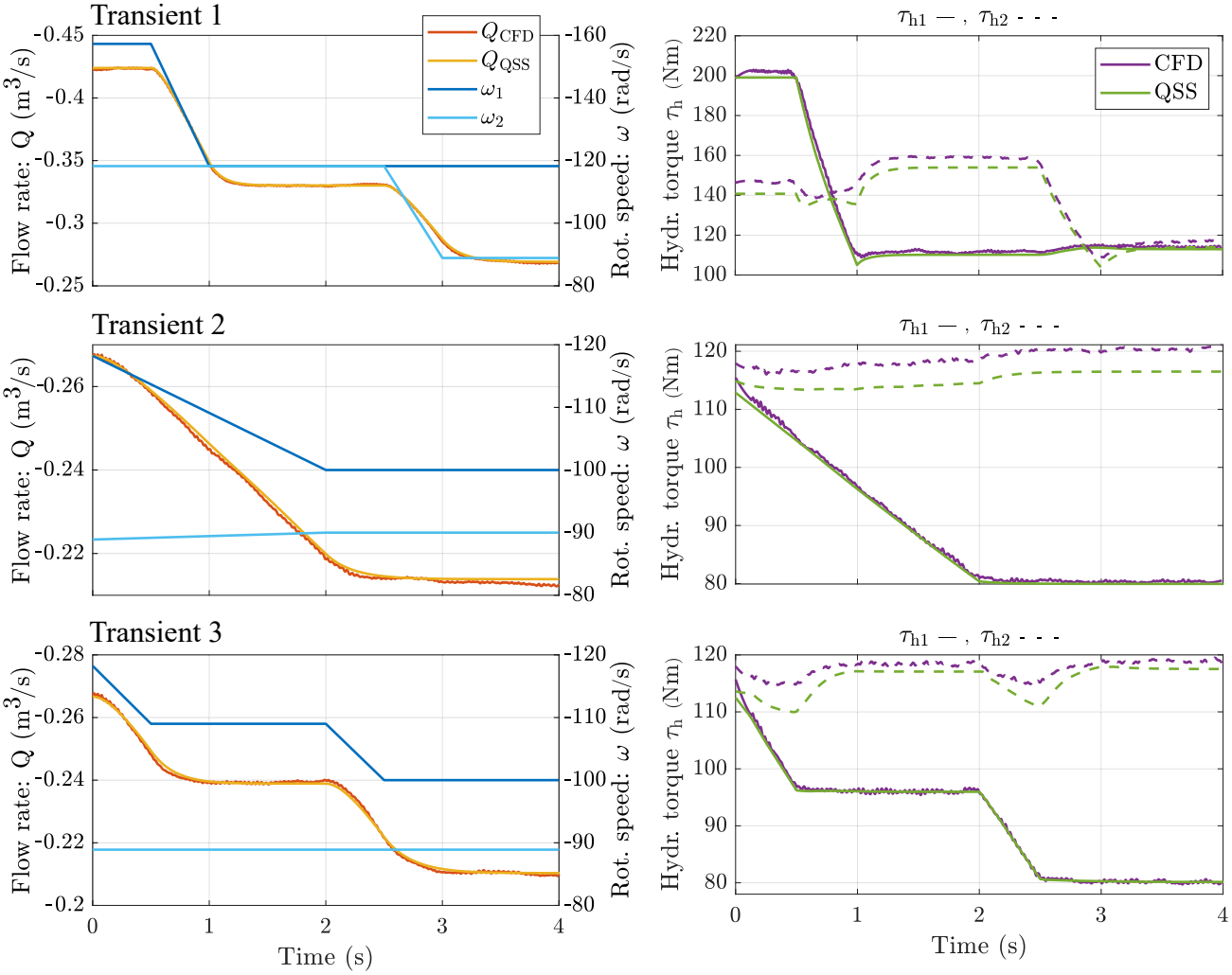

Fig. 5 Comparison between the described QSS model and CFD simulations for flow rate and hydraulic torques for three transient cases with changes in rotational speed.

With this friction torque characterisation, the rotational inertia is found by accelerating the runners up to a certain speed and then reducing the machine torque to 0 and measuring the deceleration of the runners down to standstill. With hydraulic and machine torque equal to 0, (11) is derived from (7) to find the rotational inertia, where deceleration starts at $t = T_0$ and standstill is reached at $t = T$. It is found that $J_{b1} = 0.51$ kg·m² and $J_{b2} = 1.08$ kg·m² in the hydraulic test-setup, where most of the difference is explained by the use of a 6-pole machine for runner 2 compared to a 4-pole machine for runner 1. In the emulator setup, instead of a final rotational speed of 0 rad/s, $\omega_{T1,2} = 35$ rad/s is used to avert the influence of the cogging torque occurring in the AF-PMSMs. The rotational inertia of both runners is identical in this setup: $J_{a1,2} = 1.46$ kg·m². Contrary to the friction torque, the inertia is higher in the emulator test-setup. If not accounted for, this would result in an unrealistic RPT emulator which takes more actuator effort to accelerate than the physical RPT. Following (9), in dynamic scenarios, the emulator torque $\tau_{r1,2}$ is thus adjusted based on the measured rotational speed acceleration $d\omega_{1,2}/dt$.

$$J_{1,2} \cdot [\omega_{1,2}(T_0) - \omega_{1,2}(T_{1,2})] = \int_{T_0}^{T_{1,2}} \tau_{f1,2}(t)\, dt \qquad (11)$$

Table 2 Inertia and friction torque coefficients.

Hydraulic test setup		Runner 1	Runner 2
Viscous friction coeff.	α [N·m·s]	$2.57 \cdot 10^{-2}$	$3.07 \cdot 10^{-2}$
Static friction coeff.	β [N·m]	2.49	3.59
Rotational inertia	J [kg·m²]	0.51	1.08
Emulator test setup			
Viscous friction coeff.	α [N·m·s]	$1.01 \cdot 10^{-2}$	$1.07 \cdot 10^{-2}$
Static friction coeff.	β [N·m]	1.86	1.80
Rotational inertia	J [kg·m²]	1.46	1.46

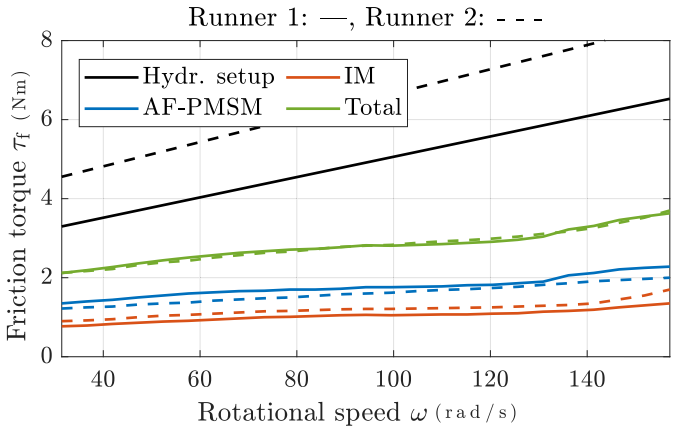

Fig. 6 Friction characterisation of the hydraulic test-setup and emulator test-setup, including its components.

4.2 Direct Torque Control Calibration

In the ABB variable frequency drives, their patented direct torque control (DTC) is used to convert the torque setpoints into switching signals for the drives [15]. In DTC, the torque and stator flux are controlled by switching between stator voltage vectors, forming the stator flux vector, which interacts with the rotor flux. A lookup table is consulted based on the torque and flux references and the current flux vector position to select the optimal voltage vector. To respectively increase/decrease torque, a voltage vector is chosen that increases/decreases the angle between stator and rotor flux. Figure 7 visualises the control schematic. Based on the measured phase voltages, currents, switch states and DC bus voltage, the torque and stator flux are found using an estimator based on an adaptive internal machine model. These estimated values are compared to the torque and flux setpoints. Hysteresis controllers then determine the proper voltage vector from a lookup table, resulting in the switching signals [2].

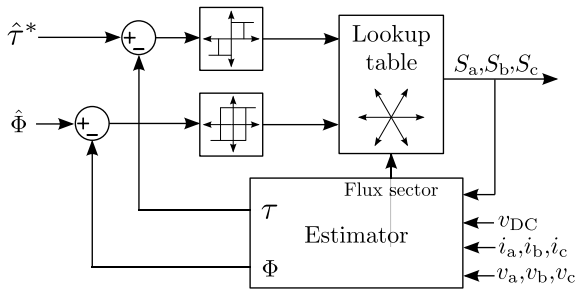

Fig. 7. Internal control schematic of DTC.

Note that the performance of this control method relies heavily on the estimator block. Therefore, any inaccuracies in the internal motor model result in an error on the machine torques compared to their setpoint values. In the VFDs, this model is based on external information about the machine nameplate parameters and internally auto-tuned using a motor identification run, in which parameters such as stator resistance, mutual inductance and saturation coefficients are identified [15]. Fig. 8 plots the torque error $\varepsilon_\tau = \tau - \hat{\tau}_r$ for the first runner versus rotational speed ω_1 for different torque setpoints $\hat{\tau}_r$, where τ is the torque sensor measurement. In theory, this error should be equal to the IM friction (solid orange line in Fig. 6). However, it can be seen that the error varies significantly for varying rotational speeds and torque setpoints. In both modes, the error increases linearly with rotational speed for $\omega > 57.6$ rad/s. Furthermore, the torque error increases for larger torque setpoints, with a large proportionality seen in pump mode, where the IM is operating in generator mode. For low speeds, the relation becomes more complex, with a positive proportionality for low torque setpoints and a negative proportionality for high torque setpoints seen in pump mode. This torque error can be explained by the small inaccuracies in the DTC estimator.

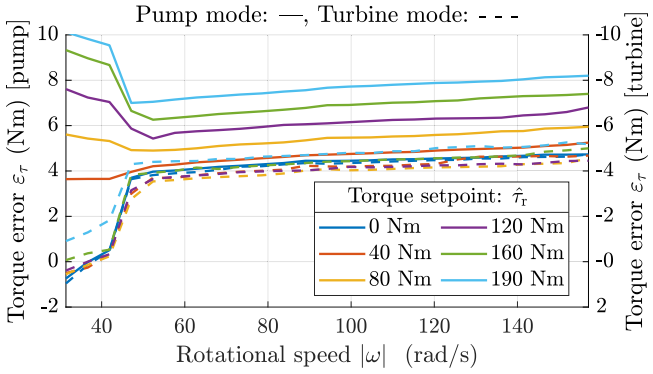

Fig. 8 The torque error $\varepsilon_\tau = \tau - \hat{\tau}_r$ versus rotational speed ω for different torque setpoints $\hat{\tau}_r$ in both pump and turbine mode.

To avert this error during emulation, a calibration module is developed that converts the actual torque setpoint $\hat{\tau}_r$ to an offset torque setpoint $\hat{\tau}_r^*$ that is known to achieve the torque setpoint $\hat{\tau}_r$ at the torque sensor. This calibration module is a 2D-lookup table with linear inter- and extrapolation, based on the measurement set shown in Fig. 8 and the measured current rotational speed.

5 Results

Fig. 9 shows the results of a test case where the AF-PMSMs are used in speed control with a standard PI-controller with clamping anti-windup. The machines are first slowed down and then sped up and the resulting emulated hydraulic torques $\tau_{h1,2}$ and runner torque setpoints $\tau_{r1,2}$ are shown. Note that the runner torque setpoints differ significantly from the original hydraulic torques during speed transients to emulate the inertial response of the CR RPT, while this difference reduces to only the friction correcting torque in steady-state. It can be seen that the speed controller of the first AF-PMSM is not optimally tuned for the decreased inertia and has significant overshoot and transient oscillations, emphasising the need for HIL test-setups to have an accurate inertia emulation to analyse controller performance. As the second runner has a lower inertia decrease compared to the emulator drivetrain, its speed

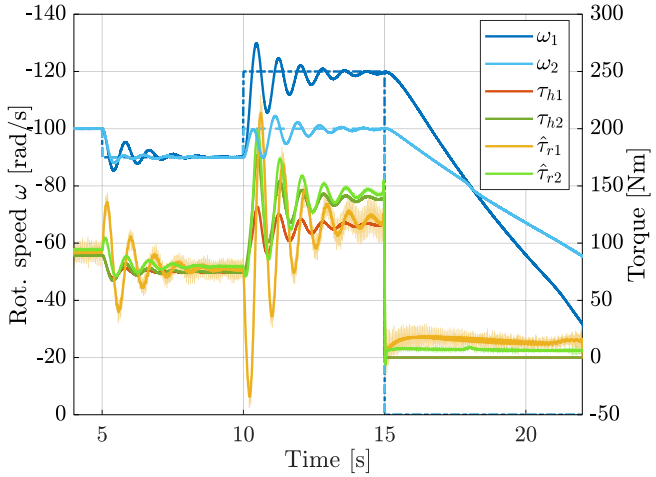

(a) Pump mode.

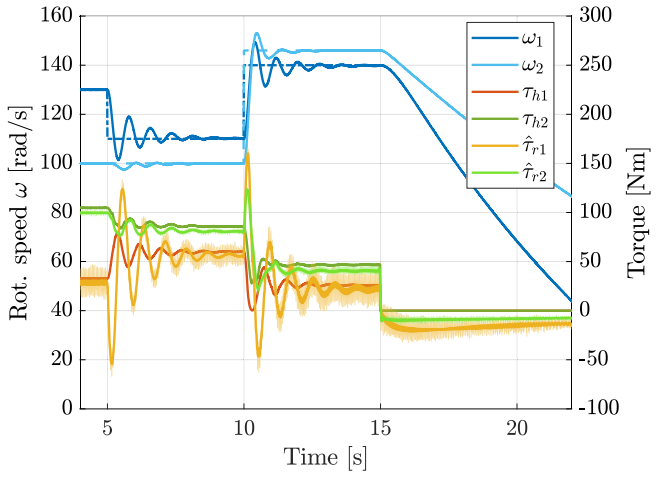

(b) Turbine mode.

Fig. 9 Emulated hydraulic torques $\tau_{\mathrm{h1,2}}$ and runner torques $\hat{\tau}_{\mathrm{r1,2}}$ for a test case where $\omega_{1,2}$ are altered by the AF-PMSMs in speed control in (a) pump mode (b) turbine mode.

response is better, and the oscillations at 10 s are caused by the high sensitivity of τ_{h2} to the oscillations of ω_1. This interaction between the two runners is further elucidated in the turbine mode case at 5 s, where only ω_1 is decreased, but the impact on τ_{h1} and ω_2 is observed. After 15 s, the AF-PMSM torque and $\tau_{\mathrm{h1,2}}$ are reduced to 0. Applying (11), the measured inertias are $J_1 = 0.45$ kg·m² and $J_2 = 1.12$ kg·m² for pump mode and $J_1 = 0.42$ kg·m² and $J_2 = 1.01$ kg·m², showing that the developed emulator manages to reliably emulate the inertia reduction.

For each of the speed setpoints in the previous test-case, the emulated runner torque setpoints $\hat{\tau}_{\mathrm{r1,2}}$, their respective calibrated values $\hat{\tau}^*_{\mathrm{r1,2}}$ and the measured torque $\tau_{1,2}$ are shown in Fig. 10. It can be seen that in all cases, the calibration manages to accurately reach a negligible error between the runner torque setpoints and the measured torques.

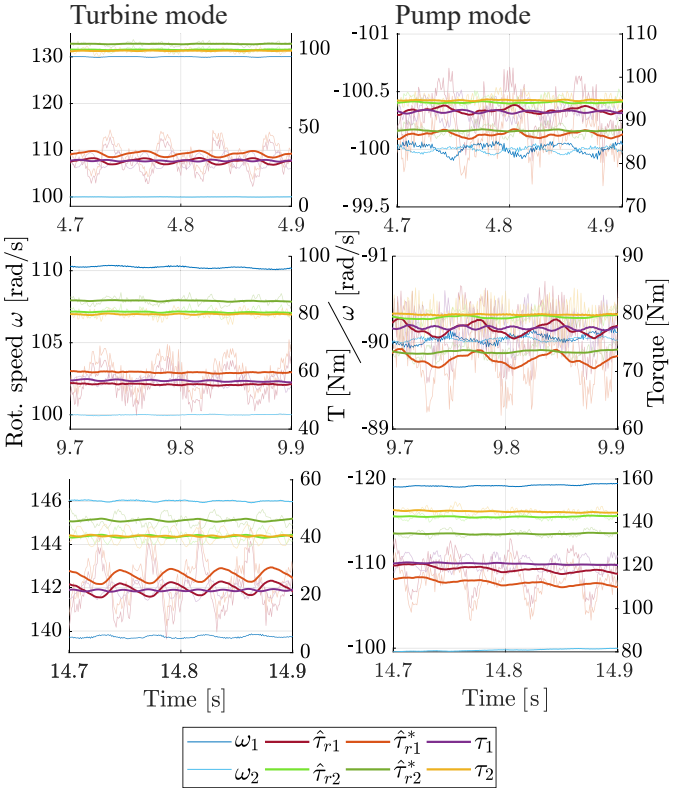

Fig. 10 DTC calibration validation for the constant speed segments in Fig. 9.

6 Conclusions

In this paper, the development of a HIL emulator test-setup for a low-head CR RPT is outlined. Here, two IMs with fully regenerative VFDs are used to emulate the two contra-rotating RPT runners in torque control. These torques are calculated at each time step based on the measured rotational speeds in an emulation model that combines the RPT and the conduit. The QSS RPT model is based on 380 steady-state CFD simulations over the full operating range. To validate the QSS model, it is compared to three transient CFD simulations in pump mode. It is found that the QSS model predicts the changes in flow rate and first runner torque accurately while the error for the second runner is larger, with an average error of 3.2%, 3.7% and 2.1% for the three cases respectively. Next, it is described how the emulator torque is altered to account for the differences in friction and inertia between the emulator test-setup and the actual RPT and its drivetrain. Finally, the torque response of the DTC used in the ABB drives is calibrated to avert the impact of estimator inaccuracies on the RPT emulation. Test results confirm the accurate emulation of the increased friction and reduced inertia of the hydraulic system compared to the HIL emulator. Furthermore, it is shown how the DTC calibration achieves a negligible error between torque setpoints and measured torque.

The developed emulator setup provides a cost-effective and controlled environment to optimise and validate control architectures for the novel CR RPT, offering a higher fidelity than pure theoretical simulation, while averting the risks associated

with testing these control strategies directly on a hydraulic setup. However, the emulator test-setup significantly benefits from the parallel hydraulic setup. Although it is found that the current QSS RPT model represents the CFD results well in dynamic scenarios, variances between the results are present, especially for the downstream runner torque. Therefore, part of the future work concerning this HIL emulator setup exists of utilising the transient test results in the hydraulic setup to train and validate a suitable data-driven model that complements the QSS model in dynamic scenarios.

7 Acknowledgements

This research is performed in context of the ALPHEUS project, which has received funding from the European Union's Horizon 2020 research and innovation programme under grant agreement No 883553. The CFD computations were enabled by resources provided by the National Academic Infrastructure for Supercomputing in Sweden (NAISS) and the Swedish National Infrastructure for Computing (SNIC) at NSC and C3SE, partially funded by the Swedish Research Council through grant agreements no. 2022-06725 and no. 2018-05973.

8 References

[1] J.-H. Kim, B.-M. Cho, S. Kim, et al. "Design technique to improve the energy efficiency of a counter-rotating type pump-turbine", *Renewable Energy*, **101**, pp. 647–659, (Feb. 2017), doi: 10.1016/j.renene.2016.09.026.

[2] J. P. Hoffstaedt, D. P. K. Truijen, J. Fahlbeck, et al. "Low-head pumped hydro storage: A review of applicable technologies for design, grid integration, control and modelling", *Renewable and Sustainable Energy Reviews*, **158**, p. 112119, (2022), doi: 10.1016/j.rser.2022.112119.

[3] J. Fahlbeck, H. Nilsson, S. Salehi, et al. "Numerical analysis of an initial design of a counter-rotating pump-turbine", *IOP Conference Series Earth and Environmental Science*, **774**, p. 012066, (June 2021), doi: 10.1088/1755-1315/774/1/012066.

[4] J. I. B. Oussama, A. F. Ben. "Performance analysis of radial and axial flux PMSM based on 3D FEM modeling", *Turkish Journal of Electrical Engineering and Computer Sciences*, **26**, pp. 1587–1598, (2018), doi: 10.3906/elk-1708-68.

[5] J. Hoffstaedt, R. Ruiz, D. Schürenkamp, ohers. "Experimental setup and methods for a novel low-head pumped storage system", *7th Offshore Energy & Storage Symposium*, pp. 341–348, (St. Julian's, Malta, 2023), doi: 10.1049/icp.2023.1589.

[6] M. Mauri, F. C. Dezza, G. Marchegiani. "A novel small-scale variable speed hydropower emulator using an inverter-controlled induction motor", *2007 European Conference on Power Electronics and Applications*, pp. 1–7, (Aalborg, Denmark, 2007), doi: 10.1109/EPE.2007.4417615.

[7] C. Rat, O. Prostean, I. Filip. "Hardware-in-the-loop emulator for a hydrokinetic turbine", *IOP Conference Series: Materials Science and Engineering*, **294**, p. 012071, (Jan. 2018), doi: 10.1088/1757-899X/294/1/012071.

[8] H. Mesnage, R. Guillaume, B. Seddik, et al. "A new real time hydraulic test platform dedicated to ancillary services", *IOP Conference Series: Earth and Environmental Science*, **774**, p. 012128, (June 2021), doi: 10.1088/1755-1315/774/1/012128.

[9] B. Guo, A. Mohamed, S. Bacha, et al. "Reduced-scale models of variable speed hydro-electric plants for power hardware-in-the-loop real-time simulations", *Energies*, **13(21)**, (2020), doi: 10.3390/en13215764.

[10] I. Moore, J. Ekanayake. "Design and development of a hardware based wind turbine simulator", *45th International Universities Power Engineering Conference UPEC2010*, pp. 1–5, (Cardiff, United Kingdom, 2010).

[11] B. M. Gavgani, A. Farnam, J. D. M. De Kooning, et al. "Efficiency enhancements of wind energy conversion systems using soft switching multiple model predictive control", *IEEE Transactions on Energy Conversion*, **37(2)**, pp. 1187–1199, (2022), doi: 10.1109/TEC.2021.3119722.

[12] U. Jassmann, M. Reiter, D. Abel. "An innovative method for rotor inertia emulation at wind turbine test benches", *IFAC Proceedings Volumes*, **47(3)**, pp. 10107–10112, (2014), 19th IFAC World Congress.

[13] I. Munteanu, A. I. Bratcu, M. Andreica, et al. "A new method of real-time physical simulation of prime movers used in energy conversion chains", *Simulation Modelling Practice and Theory*, **18(9)**, pp. 1342–1354, (2010), doi: 10.1016/j.simpat.2010.05.007.

[14] J. Fahlbeck, H. Nilsson, S. Salehi. "A head loss pressure boundary condition for hydraulic systems", *OpenFOAM Journal*, **2**, pp. 1–12, (2022), doi: 10.51560/ofj.v2.69.

[15] ABB drives. "Technical guid No.1: Direct torque control - the world's most advanced AC drive technology", Technical report, Asea Brown Boveri, (2011), URL `https://library.e.abb.com/public/14f3a3ad8f3362bac12578a70041e728/ABB_Technical_guide_No_1_REVC.pdf`.